FUDMA Journal of Sciences (FJS)
ISSN online: 2616-1370
ISSN print: 2645 - 2944
Vol. 10 No. 10, May, 2026, pp 190 – 201
DOI: https://doi.org/10.33003/fjs-2026-1010-5198

GNSS/Levelling-Based Assessment of Vertical Deformation along the Jonathan Bypass Airport Road, Calabar (Nigeria), Using the 3-Sigma Statistical Criterion

***[1]Lucas Olu Atoki; [2]Echeng Isaac Edoki; [3]Ojodugbowa Shedrack Omachoko; [1]Korede Samuel Buraimoh; [4]Sikiru Temitope Ibraheem; [1]Emmanuel Oluwayinka Akinwale; [1]Oluwagbotemi Odesola**

[1]Surveying and Geoinformatics Programme, Bowen University, Iwo, Osun State, Nigeria.
[2]Surveying and Geoinformatics, Federal Polytechnic Ugep, Cross Rivers State, Nigeria.
[3]Surveying and Geoinformatics, Bells University of Technology, Ota, Ogun State, Nigeria
[4]Geoinformatics and Surveying, University of Nigeria, Nsukka, Enugu State, Nigeria.

*Corresponding authors' email: Lucas.atoki@bowen.edu.ng
ORCID: https://orcid.org-0009-0000-8013-6845

ABSTRACT

Recently, urban areas have seen a rise in road subsidence accidents, endangering citizens. Detecting structural movement early means catching small movements, allowing for timely intervention. Various high-precision methods have been tested and implemented to mitigate these risks. This study uses the 3-sigma rule to isolate outliers and detect deformation. It combines GNSS and leveling techniques to determine vertical deflection, identifying areas prone to cave-ins and correlating them with road surface deformation. The study derived optimal Deflection of Vertical (DoV) along Calabar's Airport Road with millimeter accuracy, using geodetic coordinates (ϕ, λ, h) and orthometric height (H). The 3-sigma test showed an SD of less than 4mm and DoV of less than 4mm, indicating inliers. Correlation analysis of DoV revealed moderate positive correlation (0.460) 2022-2023, strong positive correlation (0.802) 2022-2024, and moderate positive correlation (0.551) 2023-2024. The study has demonstrated the effectiveness of GNSS and leveling techniques in monitoring road deformation, thereby highlighting areas of significant change in Calabar's Airport Road profiles. Alternative methods, such as GNSS/leveling techniques, are recommended for obtaining reliable, high-quality DoV data. These methods offer solutions to the high costs of gravimeters and satellite data resolution limitations in Nigeria, exacerbated by the economic downturn.

Keywords: Deformation; Road profiles; GPS/leveling; 3-Sigma rule; Deflection of the Vertical; Calabar's Airport Road

INTRODUCTION

Tectonic forces alter the Earth's crust, creating faults, folds, and other structures (USGS, 2019; Ogidi et al., 2021). This occurs as lithospheric plates move, accumulate stress, and deform the crust. The Calabar Flank, part of the Niger Delta Basin, has experienced significant deformation due to rifting, subsidence, and sedimentation (Battaglia & Hill, 2009; Yin & Xu, 2017).

The Calabar Flank's tectonic evolution is tied to the South Atlantic Ocean's opening, separating Africa and South America (Johnson et al., 2019; Sibson, 2002). This led to rift basin formation, including the Calabar Flank, dominated by extensional tectonics (Edoki, Ono, & Atoki, 2024a). Subsidence and sedimentation in the Cretaceous and Tertiary periods further shaped the area (Gorges et al., 2017; Johannesson & Speckert, 2013; Karlson, 2007). Geospatial technologies like remote sensing and GIS now enable better mapping and analysis of crustal deformation (Asfaw et al., 2020; Edoki et al., 2024b).

The Goodluck Jonathan Calabar road profile has developed corrugated surfaces, posing a threat to commuters, especially trailer drivers, and increasing the risk of sinkholes (Shu et al., 2014). Numerical models have shown that subsidence in urban areas is often caused by a combination of factors, including excessive groundwater extraction, natural soil consolidation, construction loads, and tectonic activities (Parkasiewicz & Kadela, 2021; Nton et al., 2018). Land subsidence in urban areas has various impacts, categorized into infrastructure, environmental, economic, and social effects. Visible signs include road cracking (Figure 2), causing vehicle vibrations that affect wear, comfort, safety, and fuel consumption. Road roughness also leads to deterioration (Ngwangwa et al., 2010). This prompted the World Bank's 1986 international road roughness experiment to standardize measurements and evaluation methods (Abulizi et al., 2016). This study examines deformation extent and road maintenance conditions, as road roughness impacts traffic safety and speed limits. Vehicle engineers use road roughness data for applications like active suspension systems (Tudón-Martínez et al., 2015). Various studies estimate road profiles from vehicle responses using techniques like artificial neural networks (ANN), as seen in Ngwangwa et al. (2010) and Yousefzadeh et al. (2010). However, ANN requires significant computational effort and large training datasets, limiting its online application.

Burger (2013) estimated road profiles by formulating an inverse control problem, it was solved using control constraints and differential-algebraic equations. Harris et al. (2010) applied mathematical optimization techniques. Speckert et al. (2014) developed a virtual measurement campaign, scoring real roads for curviness, hilliness, and roughness. Studies on Seoul, Korea, show increasing road subsidence, with 4700 cave-ins from 2010-2016 (Lee et al., 2023, 2022; Kim, 2014). (Dong et al., 2015; Okiwelu et al., 2010) examined how highway design features impact truck-involved crashes. The zero-inflated negative-binomial (ZINB) model effectively described this relationship, offering a better fit, parameter estimates, significant factors, and prediction accuracy.

This study applies the 3-sigma (3σ) rule to assess the deformation impact on Goodluck Jonathan Calabar road. With increasing road collapses and accidents in urban areas, managing underground facilities is gaining national interest. Gravity anomaly measurements show high values in areas

with unconsolidated rocks overlying basement, indicating varying subsurface conditions (Nyaberi, 2023; Zulqranan et al., 2024). Edoki et al. (2024a & b) used Sentinel-1 satellite data to characterize crustal deformation in the Calabar Flank, identifying subsidence, normal movement, and uplift with varying displacement rates. Epuh et al. (2022) and Zhang et al. (2022) assessed structural deformation and sediment accumulation in the Niger Delta Basin, integrating GRACE, Landsat 8, and ALOS data. They revealed large-scale block faults, graben topography, and growth faulting with differential subsidence dominating the basin. This study examines the deformation impact on Calabar's Goodluck Jonathan bypass road using GPS/Leveling techniques. Monthly observations from GNSS and level instruments over 3 years (2022-2024) are evaluated using the 3-sigma (3σ) rule. Similar research, like Tavakoli et al. (2009), used GPS campaigns, leveling, and gravimetry to study tectonic deformation in Iran. Dumka et al. (2022) and Kadirov et al. (2024) analyzed GPS data from 2009-2016 to study NSL's geodynamic characteristics, calculating deformation, crustal strain, and slip deficit from GPS velocities. Albayrak et al. (2024) applied geodetic astronomy and GNSS/Leveling methods for geoid determination. This study aims to assess deformation by determining deflection of the vertical using GPS/Leveling with a 3-sigma test, potentially substituting for the costly gravimetric data, looking at Nigeria's current economic challenges.

Study Area

The Calabar Flank is part of Nigeria's continental margin, located between latitudes 5°00′-5°15′N and longitudes 8°15′E-8°30′E (Figure 1). Initially part of the Lower Benue Trough, it's now a distinct basin, bounded by NW-SE faults and the Cameroon volcanic ridge. It's similar to basins in Cameroon, Gabon, Congo, and Angola, and its origin is linked to the South Atlantic opening (Edoki et al., 2024a).

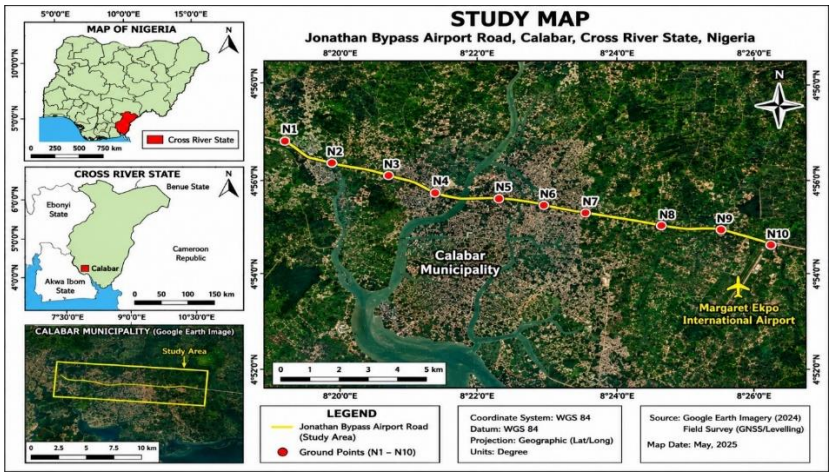

Figure 1: The Study Area (Source: author)

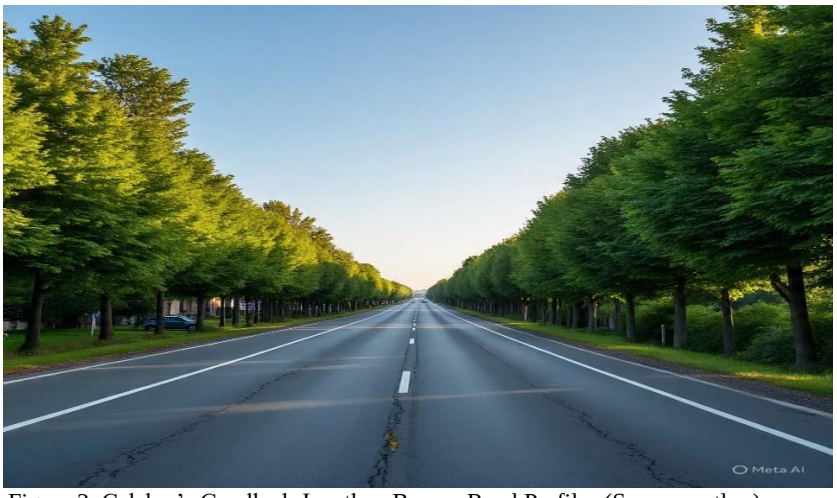

Figure 2: Calabar's Goodluck Jonathan Bypass Road Profiles (Source: author)

3-sigma (3σ) Rule a Viable Outlier Detection

Outliers are those observations that are inconsistent with the rest of the sample, often degrading estimated parameter quality and reliability. The 3σ rule is a widely used heuristic for outlier detection (Lehmann, 2013), defining outliers based on normalized residuals (Hekimoglu & Koch, 2000). It's applied in geodesy, e.g., validating the AUSGeoid98 model (Featherstone & Morgan, 2007).

About 68% of normal data falls within the most probable value (MPV) ± standard deviation, mathematically expressed as,

$$68\% \text{ of } x = \epsilon\ (\bar{x} \pm \boldsymbol{\sigma}) \quad (1)$$

The 3σ rule indicates that about 99% of normal data falls within the MPV ± 3 standard deviations, mathematically expressed as,

$$99\% \text{ of } x = \epsilon\ (\bar{\mathbf{x}} \pm \mathbf{3}\boldsymbol{\sigma}) \quad (2)$$

Determine the most probable value (MPV) of the observations.

$$\bar{x} = \frac{\sum_{i=1}^{n} x}{n} = \frac{x1+x2+\cdots+xn}{n} \quad (3)$$

Determine the standard deviation (SD) of the set of observation

$$\sigma = \sqrt{\frac{\sum_{i=1}^{n}(x1-\bar{x})2}{n-1}} \quad (4)$$

Apply the 3σ rule to determine outliers.

99% of $x = \epsilon\ (\bar{\mathbf{x}} \pm \mathbf{3}\boldsymbol{\sigma})$ (5)

Observations outside the defined range are classified as outliers.

For the 3-sigma rule to be effective, observations should be split into two parts. The first part, with many normal observations, establishes the system's statistics, unbiased by deformation errors. This can be temporally or spatially separated from the second part. For example, initial observations are taken before deformation starts, or simultaneous observations are made at a stable site nearby. The first part establishes normal observation statistics to identify outlier errors in deforming points (Ratt et al., 2015).

Deflection of the Vertical by GNSS Observation and Leveling Technique

This method was first proposed by Soler, et al (1989), where vertical deflection is found by finding the difference in the geoidal and ellipsoidal slopes. Knowing the slope of the ellipsoid and the slope of the geoid at the solution station, the deflection of the vertical is the difference in the normal to both surfaces at the geoid.

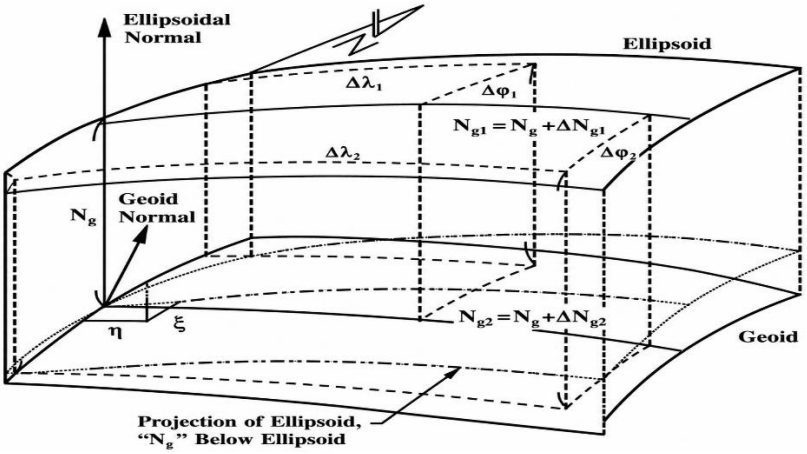

Figure 3: Geometry of the Leveling Model, (VandenBerg, 1999)

This model requires orthometric heights or height differences for each station. Given changes in geodetic coordinates (Δλ, Δϕ, h) and geoid undulation (ΔNg), the geoid's slope relative to the ellipsoid can be calculated (Figure 3). Soler et al. (1989) provide derivations using geometric and physical geodesy formulas, starting with the first eccentricity (Equ. 6).

$$e^2 = 2 \times f - f^2 \quad (6)$$

Nigeria's geodetic network consists of triangulation chains and traverse controls, computed on the Minna B datum. Established using astrogeodetic methods at station L40 (Minna base), it's a local datum based on the Clarke 1880 ellipsoid (a = 6378249.145m, f = 1/293.465) (Uzodinma et al., 2013).

The constant of latitude, required for radii of curvature on an ellipsoid of revolution, is defined as:

$$w = (1 - e^2 \times sin^2(\phi))^{1/2} \quad (7)$$

Meanwhile, the radius of curvature in the prime vertical plane (N) and the radius of curvature in the meridian plane (M) are given as;

The radius of curvature in the plane of the meridian (see equ.8)

$$R_M = \frac{a(1-e^2)}{w^3} \quad (8)$$

While equation (9) gives the radius of curvature in the plane of the prime vertical

$$R_N = \frac{a}{w} \quad (9)$$

From physical geodesy, geoidal undulation (N) is given by:

$$N_1 = h_1 - H_1 \quad (10)$$

$$N_2 = h_2 - H_2 \quad (11)$$

This equation applies to changes in geoidal undulation (ΔN), as shown in equation (12) (Soler et al., 1989; Ceylan, 2009).

$$\Delta N_{1,2} = \Delta h_{1,2} - \Delta H_{1,2} \quad (12)$$

η component of vertical deflection is computed using equation (13), having known the curvature in the east-west direction and the variation in geoid undulation with changes in longitude (slope in the longitude direction).

$$\eta = -\frac{1}{(R_N+h)\times cos\phi} \times \frac{\Delta N}{\Delta \lambda} \quad (13)$$

Likewise, ξ, was computed knowing the curvature in the meridian plane and the variation in geoid undulation with changes in latitude (slope in the latitude direction).

$$\xi = -\frac{1}{(R_M+h)} \times \frac{\Delta N}{\Delta \phi} \quad (14)$$

Meanwhile as shown in fig4, the total deflection of vertical, i.e. the angle ϑ between the plumb line and the ellipsoidal normal, is given

$$\vartheta = \sqrt{\xi^2 + \eta^2} \quad (15)$$

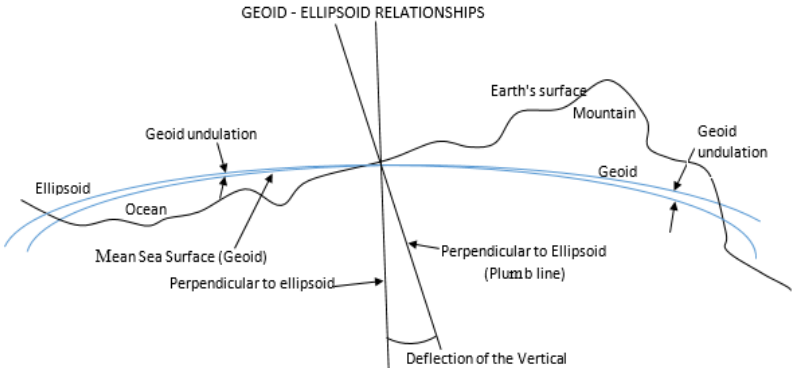

Figure 4: Deflection of the Vertical

MATERIALS AND METHODS

Deflection of the Vertical Calculation using GNSS and Leveling Observation.

The procedure in section 1.2 determines vertical deflection along the Calabar's Goodluck Jonathan bypass and road profiles (Figure 4), crucial for understanding the gravity field and geoid. Hi-Target GNSS receivers determined ellipsoidal coordinates (latitude (ϕ), longitude (λ), and height (h)) at ground control points (GCPs). Ellipsoidal height (h) is above a reference ellipsoid. Orthometric height (H) was determined using leveling instruments at the same GCPs, representing height above the geoid (mean sea level) (Liu & Zhang, 2020). Geoidal undulation (N) was calculated using equations (10 and 11), representing the difference between the ellipsoid and geoid (Figure 4). With N, deflection of the vertical (ξ, η) was determined at each point, representing the difference between actual and normal gravity vectors. This understanding of the gravity field and geoid supports geodetic applications like GPS and leveling, providing insights into subsurface density and geological structures. The process is summarized in Figure 5.

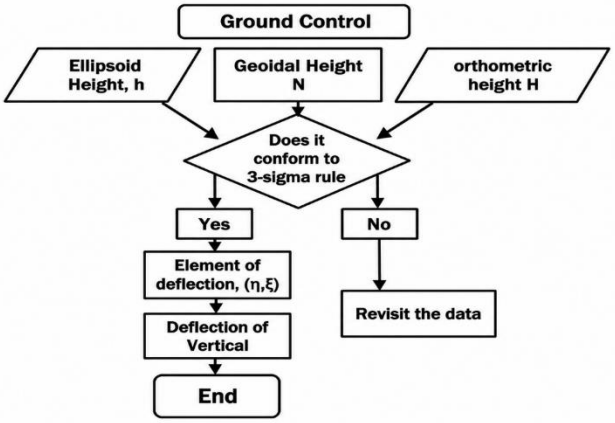

Figure 5: Flowchart of the Study

RESULTS AND DISCUSSION

Tables 3 and 4 show results of differential GNSS static positioning using Leica level instrument and Hi-Target GNSS dual-frequency receiver. Equipment specifications and configurations were studied, and initial checks were performed for optimal results. GNSS data were processed online through AUSPOS using Bernese software version 5.2. Ten ground points (h1-h10) were observed for minimum of 2 hours each, with results in Cartesian (X, Y, Z) and geodetic (latitude, longitude, ellipsoidal height) coordinates (ITRF 2020 datum). Ellipsoidal heights are in Tables 1, 3, and 5. Corresponding level observations and reduced levels are in Tables 2, 4, and 6.

Table 1: ITRF2020 Coordinates from GNSS Static processed by AUSPOS (Year 2022)

Year 2022: Ellipsoidal Height (h)										
Month	**h1**	**h2**	**h3**	**h4**	**h5**	**h6**	**h7**	**h8**	**h9**	**h10**
Jan	228.230	229.940	231.050	230.060	229.870	230.490	231.00	231.050	230.960	230.980
Feb	228.210	230.920	231.040	230.040	229.860	230.500	231.00	231.080	230.950	230.960
Mar	228.230	229.950	231.010	230.060	229.870	230.480	231.01	231.080	230.920	230.970
Apr	228.240	229.980	231.070	230.030	229.880	230.510	231.00	231.050	230.960	230.970
May	228.270	229.950	231.040	230.050	229.850	230.540	231.01	231.040	230.950	230.970
Jun	228.230	229.970	231.050	230.030	229.850	230.480	231.00	231.050	230.960	230.980
Jul	228.260	229.910	231.050	230.060	229.870	230.500	231.01	231.040	230.930	230.960
Aug	228.250	229.960	231.030	230.040	229.880	230.560	231.03	231.070	230.930	230.970
Sep	228.180	229.930	231.040	230.060	299.880	230.480	230.99	231.060	230.910	230.990

Oct	228.270	229.970	231.060	230.050	229.870	230.550	231.00	231.060	230.960	230.980
Nov	228.250	229.880	231.040	230.060	229.880	230.500	231.00	231.050	230.950	230.980
Dec	228.260	229.910	231.060	230.050	229.860	230.500	230.99	231.040	230.930	230.980

Table 2: Level Observation (Year 2022)

Year 2022: Orthometric Height (H)										
Month	**H1**	**H2**	**H3**	**H4**	**H5**	**H6**	**H7**	**H8**	**H9**	**H10**
Jan	60.8510	62.5523	63.6628	62.6746	62.4829	63.1092	63.616	63.6649	63.5747	63.5949
Feb	60.8289	62.5348	63.6592	62.6584	62.4777	63.1178	63.62	63.6932	63.5698	63.5804
Mar	60.8447	62.5642	63.6222	62.6772	62.4908	63.1007	63.622	63.6943	63.5337	63.5909
Apr	60.8518	62.6004	63.6819	62.6434	62.5005	63.1223	63.614	63.6705	63.5771	63.5890
May	60.8901	62.5691	63.6544	62.6683	62.4699	63.1551	63.624	63.6599	63.5640	63.5888
Jun	60.8482	62.5883	63.6654	62.6489	62.4811	63.1003	63.613	63.6633	63.5731	63.6008
Jul	60.8732	62.5276	63.6702	62.6734	62.4899	63.1144	63.631	63.6598	63.5503	63.5799
Aug	60.8661	62.5728	63.6498	62.6588	62.4975	63.1802	63.644	63.6888	63.5498	63.5898
Sep	60.7999	62.5496	63.6607	62.6721	62.5011	63.0999	63.611	63.6773	63.5295	63.6018
Oct	60.8822	62.5817	63.6782	62.6709	62.4819	63.1662	63.619	63.6802	63.5781	63.5927
Nov	60.8699	62.4998	63.6588	62.6801	62.4996	63.1147	63.614	63.6668	63.5707	63.5944
Dec	60.8717	62.5229	63.6806	62.6674	62.4792	63.1202	63.61	63.6595	63.5448	63.5993

Table 3: ITRF2020 Coordinates from GNSS Static processed by AUSPOS (Year 2023)

Year 2023: Ellipsoidal Height(h)										
Month	**h1**	**h2**	**h3**	**h4**	**h5**	**h6**	**h7**	**h8**	**h9**	**h10**
Jan	228.2300	229.9500	231.04	230.0600	229.87	230.49	231.01	231.04	230.96	230.9900
Feb	228.2000	229.9300	231.05	230.0500	229.87	230.49	231.00	231.07	230.95	230.9700
Mar	228.2300	229.9600	231.01	230.0600	229.9	230.49	231.01	231.08	230.92	230.9700
Apr	228.2300	229.9700	231.05	230.0300	229.87	230.51	231.01	231.06	230.93	230.9700
May	228.2700	229.9600	231.04	230.0500	229.86	230.54	231.00	231.05	230.95	230.9700
Jun	228.2400	229.9700	231.04	230.0400	229.86	230.49	231.00	231.05	230.96	230.9800
Jul	228.2600	229.9300	231.05	230.0600	229.87	230.5	231.02	231.04	230.94	230.9600
Aug	228.2500	229.9500	231.04	230.0400	229.88	230.55	231.03	231.06	230.93	230.9700
Sep	228.1800	229.9400	231.06	230.0500	229.9	230.48	230.99	231.06	230.92	230.9700
Oct	228.2600	229.9700	231.05	231.0600	229.86	230.54	231.01	231.06	230.96	230.9800
Nov	228.2800	229.8900	231.05	231.0600	229.88	230.5	231.00	231.06	230.96	230.9800
Dec	228.2600	229.9200	231.06	231.0500	229.86	230.5	231.00	231.05	230.93	230.9800

Table 4: Level observation (Year 2023)

Year 2023: Orthometric Height(H)										
Month	**H1**	**H2**	**H3**	**H4**	**H5**	**H6**	**H7**	**H8**	**H9**	**H10**
Jan	60.8441	62.5672	63.6599	62.6811	62.4844	63.1112	63.626	63.6608	63.5755	63.6018
Feb	60.8167	62.5443	63.6712	62.6621	62.4832	63.1108	63.62	63.6887	63.5683	63.5821
Mar	60.8489	62.5784	63.6289	62.6741	62.5198	63.1066	63.624	63.6914	63.5377	63.5911
Apr	60.8498	62.5903	63.6669	62.6439	62.4888	63.1217	63.622	63.6732	63.5459	63.5884
May	60.8891	62.5811	63.6601	62.6668	62.4722	63.1562	63.619	63.6631	63.5688	63.5839
Jun	60.8576	62.5879	63.6562	62.6552	62.4782	63.1014	63.613	63.6668	63.5752	63.5992
Jul	60.8802	62.5433	63.6698	62.6766	62.4885	63.1158	63.633	63.6545	63.5558	63.5786
Aug	60.8681	62.5654	63.6533	62.6592	62.4996	63.1662	63.645	63.6794	63.5511	63.5912
Sep	60.8002	62.5566	63.6745	62.6673	62.5126	63.1008	63.61	63.6788	63.5347	63.5899
Oct	60.8776	62.5826	63.6699	62.6744	62.4797	63.1588	63.622	63.6776	63.5775	63.5942
Nov	60.8919	62.5111	63.6622	62.6798	62.5006	63.1166	63.612	63.6723	63.5719	63.5951
Dec	60.8754	62.5324	63.6788	62.6668	62.4785	63.1199	63.612	63.6634	63.5457	63.5978

Table 5: ITRF2020 Coordinates from GNSS Static processed by AUSPOS (Year 2024)

Year 2024: Elipsoidal Height (h)										
Month	**h1**	**h2**	**h3**	**h4**	**h5**	**h6**	**h7**	**h8**	**h9**	**h10**
Jan	228.2400	229.9300	231.05	230.0500	229.87	230.5	231	231.04	230.95	230.9600
Feb	228.2100	229.9200	231.06	230.0500	229.86	230.51	231.01	231.06	230.95	230.9600
Mar	228.2300	229.9500	231.01	230.0600	229.88	230.49	231	231.07	230.92	230.9800
Apr	228.2400	229.9800	231.05	230.0500	229.89	230.51	231	231.05	230.96	230.9600
May	228.2700	229.9400	230.05	230.0500	229.85	230.54	231.01	231.04	230.94	230.9700

Year 2024: Elipsoidal Height (h)										
Month	**h1**	**h2**	**h3**	**h4**	**h5**	**h6**	**h7**	**h8**	**h9**	**h10**
Jun	228.2300	229.9700	231.04	230.0400	229.86	230.49	231	231.04	230.96	230.9900
Jul	228.2700	229.9100	231.05	230.0500	229.88	230.5	231.01	231.05	230.93	230.9600
Aug	228.2500	229.9300	231.03	230.0500	229.88	230.55	231.02	231.06	230.94	230.9700
Sep	228.1900	229.9300	231.04	230.0600	229.86	230.48	231	231.06	230.91	230.9900
Oct	228.2600	229.9700	231.06	230.0600	229.87	230.53	231	231.06	230.96	230.9700
Nov	228.2500	229.8900	231.04	230.0700	229.88	230.5	230.99	231.05	230.95	230.9800
Dec	228.2600	229.9100	231.06	230.0500	229.86	230.5	231	231.04	230.94	230.9800

Table 6: Level observation (Year 2024)

Year 2024: Orthometric Height(H)										
Month	**H1**	**H2**	**H3**	**H4**	**H5**	**H6**	**H7**	**H8**	**H9**	**H10**
Jan	60.8534	62.5439	63.6663	62.6684	62.4833	63.1172	63.621	63.6595	63.5686	63.5784
Feb	60.8301	62.5382	63.6782	62.6622	62.4765	63.1236	63.622	63.6797	63.5648	63.5812
Mar	60.8455	62.5652	63.6288	62.6749	62.4921	63.1062	63.62	63.6894	63.5361	63.5918
Apr	60.8555	62.5988	63.6682	62.6677	62.5027	63.1244	63.615	63.6698	63.5766	63.5777
May	60.8883	62.5609	63.6446	62.6681	62.4711	63.1542	63.627	63.6611	63.5572	63.5815
Jun	60.8478	62.5875	63.6589	62.6562	62.4773	63.1046	63.616	63.6586	63.5766	63.6013
Jul	60.8822	62.5277	63.6688	62.6658	62.4914	63.1208	63.628	63.6676	63.5499	63.5785
Aug	60.8656	62.5768	63.6494	62.6613	62.4923	63.1634	63.639	63.6806	63.5523	63.5876
Sep	60.8112	62.5459	63.6567	62.6754	62.4789	63.0986	63.613	63.6768	63.5277	63.6109
Oct	60.8793	62.5823	63.6748	62.6722	62.4822	63.1479	63.615	63.6806	63.5794	63.5899
Nov	60.8694	62.5016	63.6612	62.6814	62.4926	63.1206	63.61	63.6626	63.5712	63.5921
Dec	60.8728	62.5244	63.6747	62.6614	62.4812	63.1177	63.616	63.6588	63.5518	63.6002

Data Analysis

With reference to equ.16, the geoidal undulations are derived using the ellipsoidal height (h) from GNSS observation and orthometric height (H) from level observation. In which the most probable values and the standard deviations of the set of observations from January to December for each year are determined, as shown in Table 7, Table 8, and Table 9, respectively.

Table 7: Geiodal Undulation Calculation for the year 2022

Year 2022: Geiodal Undulation										
Month	**N1**	**N2**	**N3**	**N4**	**N5**	**N6**	**N7**	**N8**	**N9**	**N10**
Jan	167.379	167.3877	167.3872	167.3854	167.3871	167.3808	167.3844	167.3851	167.3853	167.3851
Feb	167.3811	168.3852	167.3808	167.3816	167.3823	167.3822	167.3798	167.3868	167.3802	167.3796
Mar	167.3853	167.3858	167.3878	167.3828	167.3792	167.3793	167.3878	167.3857	167.3863	167.3791
Apr	167.3882	167.3796	167.3881	167.3866	167.3795	167.3877	167.3856	167.3795	167.3829	167.3810
May	167.3799	167.3809	167.3856	167.3817	167.3801	167.3849	167.3857	167.3801	167.3860	167.3812
Jun	167.3818	167.3817	167.3846	167.3811	167.3689	167.3797	167.3866	167.3867	167.3869	167.3792
Jul	167.3868	167.3824	167.3798	167.3866	167.3801	167.3856	167.3792	167.3802	167.3797	167.3801
Aug	167.3839	167.3872	167.3802	167.3812	167.3825	167.3798	167.3859	167.3812	167.3802	167.3802
Sep	167.3801	167.3804	167.3793	167.3879	167.3789	167.3801	167.3789	167.3827	167.3805	167.3882
Oct	167.3878	167.3883	167.3818	167.3791	167.3881	167.3838	167.3807	167.3798	167.3819	167.3873
Nov	167.3801	167.3802	167.3812	167.3799	167.3804	167.3853	167.3861	167.3832	167.3793	167.3856
Dec	167.3883	167.3871	167.3794	167.3826	167.3808	167.3798	167.3801	167.3805	167.3852	167.3807
Total	2008.6023	2009.6065	2008.5958	2008.5965	2008.5679	2008.5890	2008.6008	2008.5915	2008.5944	2008.5873
$(\overline{N})$	167.3835	167.4673	167.3830	167.3831	167.3807	167.3824	167.3834	167.3826	167.3829	167.3823
σ	0.003604	0.0289111	0.003441	0.002879	0.004753	0.002912	0.003348	0.002804	0.002904	0.003308

Table 8: Geiodal Undulation Calculation for the year 2023

Year 2023: Geiodal Undulation (N)										
Month	**N1**	**N2**	**N3**	**N4**	**N5**	**N6**	**N7**	**N8**	**N9**	**N10**
Jan	167.3859	167.3828	167.3801	167.3789	167.3856	167.3788	167.3845	167.3492	167.3845	167.3882
Feb	167.3833	167.3857	167.3788	167.3879	167.3868	167.3792	167.3801	167.3113	167.3817	167.3879
Mar	167.3811	167.3816	167.3811	167.3859	167.3802	167.3834	167.3857	167.3186	167.3823	167.3789
Apr	167.3802	167.3797	167.3831	167.3861	167.3812	167.3883	167.3885	167.3368	167.3841	167.3816
May	167.3809	167.3789	167.3799	167.3832	167.3878	167.3838	167.3812	167.3369	167.3812	167.3861
Jun	167.3824	167.3821	167.3838	167.3848	167.3818	167.3886	167.3867	167.3332	167.3848	167.3808
Jul	167.3798	167.3867	167.3802	167.3834	167.3815	167.3842	167.3869	167.3655	167.3842	167.3814
Aug	167.3819	167.3846	167.3867	167.3808	167.3804	167.3838	167.3848	167.3506	167.3789	167.3788

Year 2023: Geiodal Undulation (N)										
Month	**N1**	**N2**	**N3**	**N4**	**N5**	**N6**	**N7**	**N8**	**N9**	**N10**
Sep	167.3798	167.3834	167.3855	167.3827	167.3874	167.3792	167.3801	167.3112	167.3853	167.3801
Oct	167.3824	167.3874	167.3801	168.3856	167.3803	167.3812	167.3885	167.3324	167.3825	167.3858
Nov	167.3881	167.3789	167.3878	168.3802	167.3794	167.3834	167.3883	167.3277	167.3881	167.3849
Dec	167.3846	167.3876	167.3812	168.3832	167.3815	167.3801	167.3877	167.3366	167.3843	167.3822
Total	2008.5904	2008.5994	2008.5883	2008.6027	2008.5939	2008.5940	2008.6230	2008.0100	2008.6019	2008.5967
Mean ($\overline{N}$)	167.3825	167.3833	167.3824	167.6336	167.3828	167.3828	167.3853	167.3342	167.3835	167.3831
σ	0.0025713	0.00317056	0.0029764	0.4519381	0.0031227	0.0033074	0.0031862	0.0160587	0.0023493	0.00337

Table 9: Geiodal Undulation Calculation for the Year 2024

Year 2024: Geoidal Undulation (N)										
Month	**N1**	**N2**	**N3**	**N4**	**N5**	**N6**	**N7**	**N8**	**N9**	**N10**
Jan	167.3866	167.3861	167.3837	167.3816	167.3867	167.3828	167.3792	167.3805	167.3814	167.3816
Feb	167.3799	167.3818	167.3818	167.3878	167.3835	167.3864	167.3884	167.3803	167.3852	167.3788
Mar	167.3845	167.3848	167.3812	167.3851	167.3879	167.3838	167.3803	167.3806	167.3839	167.3882
Apr	167.3845	167.3812	167.3818	167.3823	167.3873	167.3856	167.3848	167.3802	167.3834	167.3823
May	167.3817	167.3791	166.4054	167.3819	167.3789	167.3858	167.3831	167.3789	167.3828	167.3885
Jun	167.3822	167.3825	167.3811	167.3838	167.3827	167.3854	167.3842	167.3814	167.3834	167.3887
Jul	167.3878	167.3823	167.3812	167.3842	167.3886	167.3792	167.3821	167.3824	167.3801	167.3815
Aug	167.3844	167.3532	167.3806	167.3887	167.3877	167.3866	167.3812	167.3794	167.3877	167.3824
Sep	167.3788	167.3841	167.3833	167.3846	167.3811	167.3814	167.3874	167.3832	167.3823	167.3791
Oct	167.3807	167.3877	167.3852	167.3878	167.3878	167.3821	167.3852	167.3794	167.3806	167.3801
Nov	167.3806	167.3884	167.3788	167.3886	167.3874	167.3794	167.3802	167.3874	167.3788	167.3879
Dec	167.3872	167.3856	167.3853	167.3886	167.3788	167.3823	167.3837	167.3812	167.3882	167.3798
Total	2008.5989	2008.5768	2007.6094	2008.6250	2008.6184	2008.6008	2008.5998	2008.5749	2008.5978	2008.5989
Mean ($\overline{N}$)	167.3832	167.3814	167.3008	167.3854	167.3849	167.3834	167.3833	167.3812	167.3832	167.3832
σ	0.0030156	0.0092933	0.281979	0.002762	0.0036758	0.0026094	0.0028756	0.0023027	0.0028561	0.0039272

Data Test with 3-Sigma Rule

Following the Equation 3-5, the average and the standard deviation were calculated leading to the statistical analysis of 3-sigma test of the various observations carried out in different epochs.

Table 10: Most Probable Value ($\overline{N}$) and Standard Deviation Error (σ) at Each Points of the Year

Year/Point	$\overline{N}1$	$\overline{N}2$	$\overline{N}3$	$\overline{N}4$	$\overline{N}5$	$\overline{N}6$	$\overline{N}7$	$\overline{N}8$	$\overline{N}9$	$\overline{N}10$
2022	167.3835	167.4673	167.3830	167.3831	167.3807	167.3824	167.3834	167.3826	167.3829	167.3823
2023	167.3825	167.3833	167.3824	167.6336	167.3828	167.3828	167.3853	167.3342	167.3835	167.3831
2024	167.3832	167.3814	167.3008	167.3854	167.3849	167.3834	167.3833	167.3812	167.3832	167.3832
Year/Point										
	σ1	σ2	σ3	σ4	σ5	σ6	σ7	σ8	σ9	σ10
2022	0.003604	0.2891111	0.003441	0.002879	0.004753	0.002912	0.003348	0.002804	0.002904	0.003308
2023	0.0025713	0.00317056	0.0029764	0.4519381	0.0031227	0.0033074	0.0031862	0.0160587	0.0023493	0.00337
2024	0.0030156	0.0092933	0.281979	0.002762	0.0036758	0.0026094	0.0028756	0.0023027	0.0028561	0.0039272

Table 11: Data Integrity and the Range of Observations Considered to be Inliers

Year/Point	**N1**	**N2**	**N3**	**N4**	**N5**	**N6**	**N7**	**N8**	**N9**	**N10**
2022	167.37269	166.59997	167.37268	167.37446	167.36644	167.37366	167.37336	167.37419	167.37419	167.37238
	167.39431	168.33463	167.39332	167.39174	167.39496	167.39114	167.39344	167.39101	167.39161	167.39222
2023	167.37479	167.37379	167.37347	166.27779	167.37343	167.37288	167.37574	167.28602	167.37645	167.37299
	167.39021	167.39281	167.39133	168.98941	167.39217	167.39272	167.39486	167.38238	167.39055	167.39321
2024	167.37415	167.35352	166.45486	167.37711	167.37387	167.37557	167.37467	167.37429	167.37463	167.37142
	167.39225	167.40928	168.14674	167.39369	167.39593	167.39123	167.39193	167.38811	167.39177	167.39498

Table 11 shows the overall data integrity and the range of observations considered to be inliers as it was verified through the adoption of 3-sigma test (Equ.1-5) on all the geoidal undulations of points ranging from N1 to N10, nearly all the observations were considered to be inlier at all the points chosen, except for the two occasions. Looking at point N2 (February, 2022), the range of observations considered to be inliers is from 166.6000 to 168.3346, observation done by February fall (above the 3σ threshold) on outlier with the value of 168.3852. There is also same occurrence at point N3 (May, 2024), the actual range of observations considered to be inliers is from 166.4549 to 168.1467, the observation found to fall (below the 3σ threshold) on outlier with the value of 166.4054. However, all the observation done in the year 2023 were inliers. The scarcity of outliers indicates high data integrity from both GNSS and leveling campaigns, ISO (2016). Having affirmed the integrity of the data, the deduction of deflection of the vertical with the procedural equation earlier stated (session 1.2) were strictly followed.

Table12: Deflection of the Vertical Deduction

Year/Point	2022 (arcsecond)	2023 (arcsecond)	2024 (arcsecond)
9□1	0.00001240022	0.00001240016	0.0000124002
9□2	0.00001240546	0.00001239924	0.00001239909
9□3	0.00001239822	0.00001239818	0.00001239214
9□4	0.00001239638	0.00001241494	0.00001239655
9□5	0.00001239528	0.00001239538	0.00001239553
9□6	0.00001239436	0.00001239439	0.00001239444
9□7	0.00001239344	0.00001239358	0.00001239344
9□8	0.00001239264	0.00001238906	0.00001239254
9□9	0.00001239161	0.00001239165	0.00001239163
9□10	0.00001239154	0.00001239153	0.00001239154

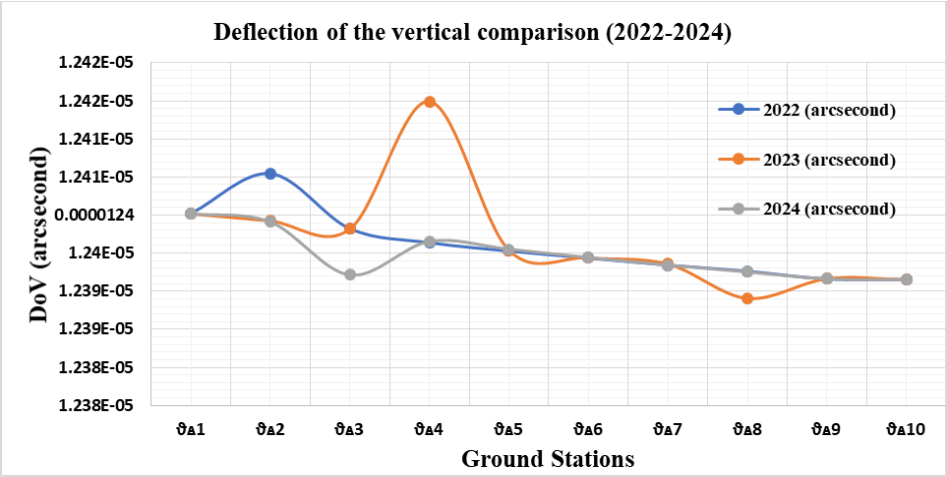

Figure 6: Deflection of Vertical (DoV) by year comparison

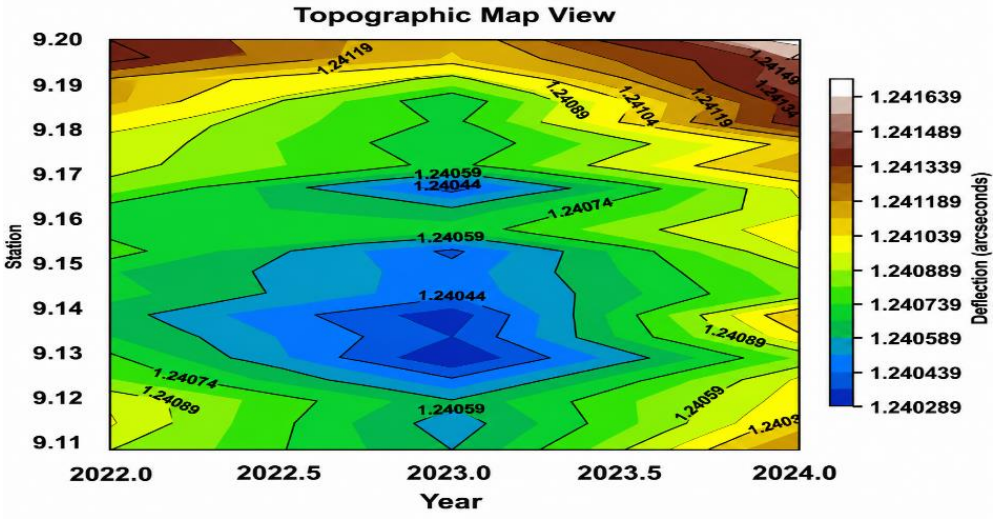

Figure 7: Profile Elevation View

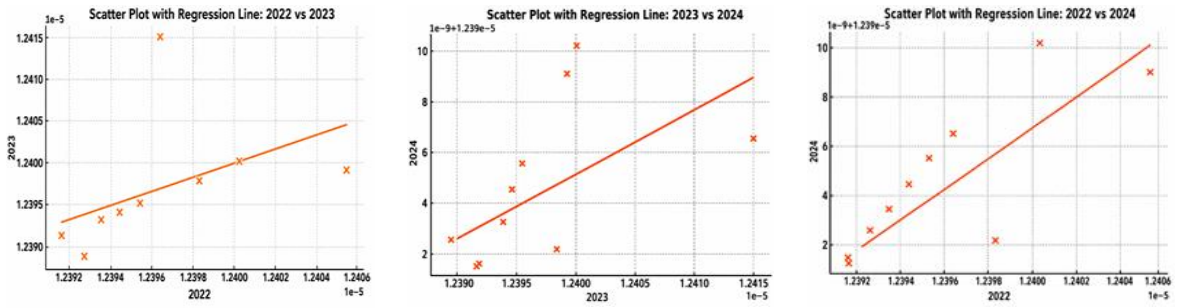

(a) (b) (c)

Figure 8: Correlation Analysis Graph (a, b, c)

Discussion

This study successfully determined the Deflection of the Vertical (DoV) using integrated GNSS/leveling observations and the 3-sigma statistical criterion to derive geoidal undulations at established monitoring points. The Calabar Goodluck Jonathan Bypass Road profile was assessed for underground deformation from 2022 to 2024 through monthly GNSS/leveling observations conducted at ten ground stations. This approach enabled the assessment of vertical movements, including subsidence, stable ground conditions, and localized uplift. The observed upward trend of the Deflection of the Vertical along the cumulative distance (Figure 6) indicates progressive spatial variation in the gravity field and surface geometry. The computation combined GNSS-derived ellipsoidal coordinates (ϕ, λ, h) with precise orthometric heights (H), following the standard GNSS/leveling methodology widely adopted for geoid determination and vertical deflection studies (Ceylan, 2009; Featherstone & Morgan, 2007; Albayrak et al., 2024).

The GNSS observations and precise leveling measurements achieved millimetre-level precision, demonstrating the suitability of the integrated approach for engineering deformation monitoring. Comparable accuracies have been reported by Ceylan (2009), who demonstrated the effectiveness of GPS/leveling for determining Deflection of the Vertical, and by Albayrak et al. (2024), who obtained centimetre- to millimetre-level geoid accuracy using GNSS/leveling integrated with geodetic astronomy. The present study therefore confirms that GNSS/leveling remains a reliable alternative for deformation assessment in regions where dense gravimetric observations are unavailable.

Geoidal undulation estimates revealed larger temporal fluctuations at monitoring points N3, N4 and N8, suggesting localized subsidence or differential settlement. Point N3 exhibited a pronounced decrease in May 2024 (166.4054 m), while Point N4 consistently showed greater temporal variability during 2023, indicating that these locations may represent localized deformation hotspots. Similar localized deformation patterns have been reported by Dumka et al. (2022), who observed heterogeneous crustal movements from continuous GPS measurements, and by Kadirov et al. (2024), who demonstrated that long-term GPS observations often reveal spatially variable deformation associated with local geological structures. Likewise, Epuh et al. (2022) linked localized crustal deformation in the Niger Delta Basin to variations in subsurface geological conditions, suggesting that similar geological controls may influence deformation within the Calabar Flank.

The application of the 3-sigma statistical criterion demonstrated high data integrity throughout the monitoring period. Nearly all observations satisfied the acceptance limits, with only two observations classified as outliers. Such performance confirms the effectiveness of rigorous statistical quality control in deformation monitoring. Similar findings have been reported by Hekimoglu and Koch (2000), who demonstrated that statistical reliability testing substantially improves confidence in geodetic observations, while Lehmann (2013) showed that appropriate outlier detection minimizes the influence of gross observational errors on deformation analysis. The two outliers identified in this study are most likely attributable to temporary GNSS observation errors, including cycle slips, multipath interference, signal obstruction, or local reflection effects, rather than persistent ground movement.

The observed standard deviations, generally below 4 mm, indicate high internal precision of the GNSS/leveling observations. This level of precision agrees with international standards for high-quality road profile measurements (ISO 8608:2016) and is comparable to precision levels reported in recent geoid determination studies using integrated GNSS/leveling techniques (Albayrak et al., 2024). Nevertheless, although statistical precision was high, systematic effects such as antenna phase-centre variations, atmospheric delays, and residual multipath cannot be completely eliminated and remain inherent limitations of high-precision GNSS observations.

The observed gentle road cave-ins between 2022 and 2024 (Figure 7) suggest progressive surface deformation that may be associated with hidden cavities, differential compaction, groundwater fluctuations, or weak subgrade conditions. Similar mechanisms have been identified as major contributors to pavement subsidence and infrastructure deterioration by Kim (2014), Lee et al. (2022), and Lee et al. (2023), who reported that underground utility conditions, soil characteristics and groundwater changes significantly influence ground subsidence in urban environments. Consequently, the localized deformation observed in this study should not be interpreted solely as evidence of crustal deformation but rather as the combined response of geological and engineering factors.

Correlation analysis revealed moderate positive correlation between the 2022 and 2023 observations ($r = 0.460$), strong positive correlation between the 2022 and 2024 observations ($r = 0.802$), and moderate positive correlation between the 2023 and 2024 observations ($r = 0.551$) (Figure 8). These relationships indicate that the overall deformation pattern remained generally consistent despite localized variations. The regression analysis similarly demonstrated relatively stable DoV values between 2022 and 2023, whereas 2024 exhibited increased fluctuations and localized distortions. Such temporal behaviour agrees with previous GNSS deformation studies, which have shown that deformation generally evolves progressively rather than abruptly under the combined influence of geological processes and environmental loading (Ding et al., 2017; Dumka et al., 2022; Kadirov et al., 2024).

Overall, the analysis indicates that the DoV field remained relatively stable between 2022 and 2023 but became more variable during 2024. The increasing regression slope across the observation periods suggests greater sensitivity of the 2024 DoV field to previous-year variations. Unlike many previous studies that focused primarily on regional crustal deformation (Dumka et al., 2022; Kadirov et al., 2024) or geoid validation (Featherstone & Morgan, 2007; Albayrak et al., 2024), the present investigation demonstrates the practical application of integrated GNSS/leveling observations for monitoring transportation infrastructure. The study therefore extends existing knowledge by showing that high-precision geodetic techniques, combined with rigorous statistical quality control, provide an effective and economical tool for detecting localized deformation along road corridors, particularly in developing countries where gravimetric surveys and continuous InSAR monitoring remain limited.

CONCLUSION

This study evaluated the vertical deformation characteristics of the Goodluck Jonathan Bypass Airport Road, Calabar, Nigeria, using integrated GNSS static observations and precise spirit leveling conducted over a three-year period (2022–2024). Geoidal undulations derived from ellipsoidal and orthometric heights were analysed using the 3-sigma statistical criterion to assess data quality prior to the determination of the Deflection of the Vertical (DoV).

The results demonstrate that the combined GNSS/leveling approach provides consistent and highly precise measurements suitable for deformation monitoring. The majority of the observations satisfied the 3-sigma criterion, confirming the reliability and integrity of the acquired data. Only two observations were identified as outliers throughout the monitoring period, indicating that the dataset was generally free from significant gross errors and suitable for deformation analysis.

The estimated Deflection of the Vertical values remained within the millimetre-level precision expected from high-quality geodetic observations. Although the overall deformation pattern was relatively stable, localized variations were observed at several monitoring stations, particularly around Points N3, N4 and N8, suggesting areas that warrant continued observation. Correlation analysis further showed moderate similarity between the 2022–2023 and 2023–2024 datasets, while a stronger correlation existed between the 2022 and 2024 observations, indicating temporal consistency in the deformation behaviour despite localized fluctuations.

The study demonstrates that integrated GNSS and precise leveling observations, supported by rigorous statistical quality control using the 3-sigma criterion, constitute an effective and economically viable technique for long-term road deformation monitoring. The methodology is particularly valuable in regions where gravimetric observations or continuous InSAR monitoring are unavailable or prohibitively expensive.

The observed localized variations should not be interpreted as conclusive evidence of crustal deformation alone, since pavement performance may also be influenced by geotechnical conditions, groundwater fluctuations, traffic loading, drainage deficiencies, and pavement material characteristics. Therefore, future investigations should integrate geotechnical testing, geophysical surveys, InSAR observations, and continuous GNSS monitoring to establish the dominant mechanisms responsible for the detected deformation and to support sustainable maintenance planning for critical transportation infrastructure.

REFERENCES

Abulizi, N., Kawamura, A., Tomiyama, K. & Fujita, S. (2016). Measuring and evaluating of road roughness conditions with a compact road profiler and ArcGIS. *Journal of Traffic and Transportation Engineering*, 3(5):398e411

Albayrak, M., Marti, U., Willi, D., Guillaume, S. & Hardy, R.A. (2024). Precise Geoid Determination in the Eastern Swiss Alps Using Geodetic Astronomy and GNSS/Leveling Methods. *Sensors*, 24, 7072. https://doi.org/10.3390/s24217072

Battaglia, M. & Hill, D.P. (2009). Analytical modeling of gravity changes and crustal deformation at volcanoes: The Long Valley caldera, California, case study. *Tectonophysics*, 471 (1–2), 45–57.

Burger, M. (2013). Calculating road input data for vehicle simulation. Multibody System of Dynamics. 31: 93–110.

Ceylan, A. (2009). Determination of the Deflection of Vertical Components via GPS and Leveling Measurement: A Case Study of a GPS Test Network in Konya, Turkey. *Scientific Research and Essay*, 4(12): 1438–1444.

Ding, L., Qin, F.C., Fang, H.D., Liu, H., Zhang, B., Shu, C.Q., Deng, Q.C., Liu, G.C. & Yang, Q.Q. (2017). Morphology and controlling factors of the longitudinal profile of gullies in the Yuanmou dry-hot valley. *Journal of Mountain Science.* 14: 674–693**,** https://doi.org/10.1007/s11629-016-4189-7

Dong, C., Nambisan, S. S., Richards, S. H. & Ma, Z. (2015). Assessment of the effects of highway geometric design features on the frequency of truck involved crashes using bivariate regression, *Transportation Research Part a Policy and Practice*, 75, https://doi.org/10.1016/j.tra.2015.03.007

Dumka, R. K. SuriBabu, D., Kotlia, B.S., Kothyari, G. C. & Prajapati, S. (2022). Crustal deformation measurements by global positioning system (GPS) along NSL, western India. *Geodesy and Geodynamics*, 13: 254-260.

Edoki, E. I., Ono, M. N. & Atoki, L. O. (2024a). Characterization and Mapping of Calabar Flank Crustal Deformation Using Sentinel -1 Data. *International Journal of Engineering Inventions*, 13(9): 88-92

Edoki, E. I., Ono, M. N. & Igwebuike, A. E. (2024b). Integrated Analysis of Gravity and Geoidal Anomalies for Understanding Crustal Deformation and Tectonic Processes in the Calabar Flank, Nigeria. *International Journal of Multidisciplinary Research and Growth Evaluation*. 5(5): 371-377

Epuh, E.E., Moshood, A.I., Okolie, C.J., Daramola, O.E., Akinnusi, S.A., Arungwa, I., Orji, M.J., Olanrewarju, H.O. & Fatoyinbo, A .A . (2022). Integration of satellite gravimetry, multispectral imagery and digital elevation model for investigating crustal deformation in the Niger Delta Basin. *Geosystems and Geoenvironment* 1(100067).

Featherstone, W. & Morgan, L. (2007). Validation of the AUSGeoid98 model in Western Australia using historic astrogeodetically observed deviations of the vertical, *Journal of the Royal Society of Western Australia*. 90(3):143-150.

Gorges, C., Öztürk, K. & Liebich, R. (2017). *Road classification for two-wheeled vehicles, Engineering Design and Product Reliability, Berlin Institute of Technology, Berlin, Germany*, http://www.tandfonline.com/10.1080/00423114.2017.1413197

Harris, N. K., González, A., OBrien E. J. & McGetrick, P. J. (2010). Characterisation of pavement profile heights using accelerometer readings and a combinatorial optimization technique. *Journal of Sound and Vibration*, 329(5) 497–508, https://doi.org/10.1016/j.jsv.2009.09.035

Hekimoglu, S., & Koch, K. R. (2000). *"How can reliability of the test for outliers be measured?"* Allgemeine Vermessungsnachrichten, 107(7): 247–253

SO. (2016). *Mechanical vibration—Road surface profiles—Reporting of measured data*. Standard No. 8608:2016. Geneva, Switzerland.

Johannesson, P. & Speckert, M. (2013). *Guide to load analysis for durability in vehicle engineering*. Chichester, Wiley, 434.

Johnson, C., Affolter, M.D., Inkenbrandt, P. & Mosher, C. (2019). *An Introduction to Geology*. Faculty (Geology) Salt Lake Community College.

Kadirov F., Yetirmishli G., Safarov R., Mammadov S., Kazimov I., Floyd M., Reilinger R. & King R. (2024). Results from 25 Years (1998-2022) Of Crustal Deformation Monitoring in Azerbaijan and Adjacent Territory Using GPS. *ANAS Transactions, Earth Sciences* 1: 28-43; https://doi.org/10.33677/ggianas20240100107

Karlsson, M. (2007). *Load modelling for fatigue assessment of vehicles – a statistical approach.* PhD thesis. Göteborg, Sweden: Chalmers, Göteborg University.

Kim, Y.R. (2014). Subsidence occurrence and countermeasure by sewer. *Water Journal*, 11: 73–78.

Lee, S.Y., Kang, J.M. & Kim, J.Y. (2022). Development of Machine Learning Model to predict the ground subsidence risk grade according to the Characteristics of underground facility. *Journal of the Korean Geo-Environmental Society*, 23: 5–10.

Lee, S., Kang, J. & Kim, J. (2023). A Study on Factors Influencing Ground Subsidence and a Risk Analysis Method Using the Attributes of Sewer Pipes. *Applied Sciences*, 13: 9714. https://doi.org/10.3390/app13179714

Lehmann, R. (2013). On the Formulation of the Alternative Hypothesis for Geodetic Outlier Detection. *Journal of Geodesy*, .87(4): 373-386.

Liu, L. & Zhang, C. (2020). Analysis of Importance of Engineering Survey in Construction Engineering Quality Management, E3S Web of Conferences 213, 03022, https://doi.org/10.1051/e3sconf/202021303022

Ngwangwa, H. M., Heyns, P. S., Labuschagne F. J. J. & Kululanga, G. K. (2010). Reconstruction of road defects and road roughness classification using vehicle responses with artificial neural networks simulation. *Jounal of Terramechanics*, 47 (2), 97–111. https://doi.org/10.1016/j.jterra.2009.08.007

Nton, M. E., Akpan, O. S. & Adamolekun, O. J. (2018). Geochemistry of Ekenkpon and Nkporo Shales, Calabar Flank, Se Nigeria: Implications for Provenance, Transportation History and Depositional Environment. *Global Journal of Geological Sciences*, 16(2018): 63-78. DOI: Http://Dx.Doi.Org/10.4314/Gjgs.V16i1.7

Nyaberi, D. M. (2023). Implications on Gravity Anomaly Measurements Associated with Different Lithologies in Turkana South Subcounty. *Journal of Geoscience and Environment Protection*, 11: 79-118. https://doi.org/10.4236/gep.2023.111006.

Ogidi, A. O., Essien N. U., Okon, E. E., Nton, M. E. & Jackson, C. A. (2021). Evaluation of the Shale Gas Potentials of Ekenkpon Shale, Calabar Flank, Southeastern Nigeria. *NAPE Bulletin 30 (1); 55-69.*

Okiwelu, A., Okwueze, E., Okereke, C. & Osazuwa, I. (2010). Crustal Structure and Tectonics of the Calabar Flank, West Africa, based on Residual Gravity Interpretation. *European Journal of Scientific Research*. 42(2): 195-203

Parkasiewicz, B. & Kadela, M. (2021). Effect of Assumed Boundary Conditions in Numerical. Model of Road Pavement-Mining Subsoil System on Criterial Values Used in Design Using Mechanistic Methods. IOP Conference Series: *Materials Science and Engineering*, 1203: 032021

Rath, J. J., Veluvolu K. C. & Defoort, M. (2015), Simultaneous estimation of road profile and tire road friction for automotive vehicle. *IEEE Transactions on Vehicular Technology*, 64(10): 4461–4471.

Shu, C. Q., Zhang, B., Jiang, L. Q., Liu, S. J., & Luo, M. L. (2014). Development Characteristics and Evolution Process of the Sink Holes in Yuanmou Dry-Hot Valley. *Trop. Geogr*, *34*: 141-147.

Sibson, R.H. (2002). *29 - Geology of the crustal earthquake source. In: Lee, W.H.K., Kanamori, H., Jennings, P.C., Kisslinger, C. (Eds.),* Int. Geophys. Academic Press, 81: 455–473

Speckert, M., Dressler, K.G., Ruf, N., Halfmann, T. & Polanski, S. (2014). *The virtual measurement campaign (VMC) concept. Commercial Vehicle Technology, Kaiserslautern, Germany*: Shaker Verlag, 88–98.

Soler T., Archie E., Calson J., & Alan G. E. (1989). Determination of Vertical Deflection using the Global Positioning System and Geodetic Leveling. *Geophysical Research Letters*. 695-698.

Tavakoli, F., Nankali, H.R., Soltanpour, A., sedighi, M., Khormi, F. & Arabi, S. (2009). *Application of Geodetic Tools for Crustal Deformation Monitoring in Iran. Eighteenth United Nations Regional Cartographic Conference for Asia and the Pacific Bangkok*, 26-29.

Tudón-Martínez, J. C., Fergani, S., Sename, O., Molina, J.J.M., Morales-Menendez, G. & Dugard, L. (2015). Adaptive road profile estimation in semi-active car suspensions. *IEEE Transactions on Control Systems Technology*, 23(6): 2293–2305.

USGS. (2019). *Tracking Stress Buildup and Crustal Deformation. Retrieved from https://www.usgs.gov/natural-hazards/earthquake- hazards/science/tracking- stress-buildup- and- crustal- deformation.*

Uzodinma, V. N. & Raphael, E. I. (2013). *Removal of Inconsistencies Arising from Multiplicity of Transformation Parameters in Nigeria*. FIG Working Week 2013 Environment for Sustainability Abuja, Nigeria. TS02B - National Geodesy and Geospatial Infrastructure II – 6552.

Yin, Z. & Xu, C. (2017). Estimating gravity changes caused by crustal strain: application to the Tibetan Plateau. *Geophys. J. Int.*, 210 (2): 1191–1205.

Yousefzadeh, M., Azadi, S. & Soltani, A. (2010). Road profile estimation using neural network algorithm. *Journal of Mechanical Science and Technology*, 24(3): 743–754.

Zhang, T., Shen, Z., He, L., Shen,W. & Li,W. (2022). Strain Field Features and Three-Dimensional Crustal Deformations Constrained by Dense GRACE and GPS Measurements in NE Tibet. *Remote Sens*. 14: 2638. https://doi.org/10.3390/rs14112638

Zulqranan, A., Šprlák, M. & Khan, M.R. (2024). *Geophysical Study of Crustal Deformation Using Gravity Data:*

Muzaffarabad and Adjoining Regions in Azad Jammu and Kashmir. Http://doi.org/10.21203/rs.3.rs-5387180/v1